Environmental Fluid Mechanics (2026) 26:21
https://doi.org/10.1007/s10652-026-10078-0

ORIGINAL ARTICLE

Effect of a vertical cylinder on gravity currents dynamics and mixing

Giovanni Di Lollo[1] · **Maria Rita Maggi**[1] · **Claudia Adduce**[1]

Received: 2 December 2025 / Accepted: 7 March 2026 / Published online: 27 March 2026

Abstract
This work investigates how a vertical cylindrical obstacle affects the dynamics and mixing of lock-release gravity currents. Gravity currents are produced in the laboratory and density fields are measured using an image analysis. Two Reynolds numbers, three submergence ratios and three flow blockage ratios have been tested. Results show that upstream of the cylinder, gravity currents propagation remains unaffected. Downstream of the obstacle, the front velocity decreases compared to the undisturbed case, with a deceleration becoming larger as the obstacle diameter increases. The deceleration does not trigger the transition from the slumping to the self-similar phase. Greater obstacle height causes an increased current thickness upstream of the cylinder, while larger diameters amplify both the thickness and the reflection of the dense current. The entrainment parameter remains unchanged across all tested configurations. Energy budget analysis reveals an enhancement of mixing in the presence of obstacles.

Maria Rita Maggi and Claudia Adduce have contributed equally to this work.

Extended author information available on the last page of the article

Graphical abstract

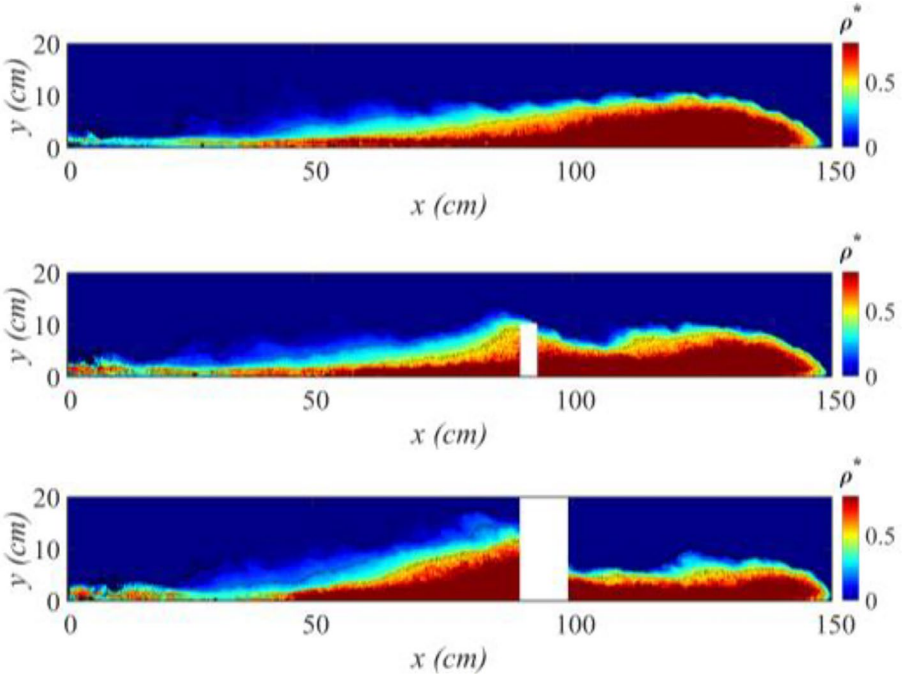

Keywords Experimental · Gravity current · Lock-release · Mixing · Vertical cylinder

1 Introduction

Horizontal buoyancy-driven currents, known as gravity currents, arise from the hydrostatic imbalance between fluids of different densities. Some of the possible density differences that drive these currents are the temperature and salinity changes experienced by ocean currents or the exchange of salt and fresh water in estuaries. The transport of pollutants into the atmosphere or oceans also takes the form of a gravity current [1]. As they travel, gravity currents interact with varying and complex ground morphology and man-made structures. The analysis of the main characteristics and dynamics of gravity currents has therefore attracted considerable scientific interest. The propagation of gravity currents on a horizontal smooth bottom has been the subject of a number of studies over the years, both laboratory experiments and numerical simulations [2–11], as well as the influence of different slopes [12–20] and the presence of bottom roughness [21–29]. In addition, gravity currents interact with a variety of obstacles, both natural and artificial ones, requiring the study of different current-obstacle interactions. Using submerged obstacles occupying the entire width of the domain and of different shapes and configurations, the influence of artificial structures on the dynamics of gravity currents has been extensively studied. The results emphasise that compared to gravity currents moving over a smooth horizontal bed, the propagation of cur-

rent fronts is slowed down due to increased drag, friction and viscous forces, as well as increased formation of turbulent structures and vortices. [30–41].

There is a lack of research on the effects induced by the presence of an isolated obstacle that does not occupy the full width of the domain. In the work of Mok et al. [42], the laser-induced fluorescence technique has been used to analyse the interaction between a gravity current and an emergent cylinder mounted perpendicular to the bottom. Three phases have been identified: an impact phase, in which the gravity current rises along the face of the obstacle; a transition phase, in which the current reaches its maximum height; and a quasi-steady phase, characterized by the descent of the current. During the first and second stages, an area of circulation is identified upstream of the obstruction as the result of the interaction between the rised dense current and the return flow of ambient fluid. Di Lollo et al. [43] performed two-dimensional velocity field measurements using Particle Image Velocimetry of a gravity current interacting with a vertically emergent cylinder, before impact. The analyses showed how the presence of the cylinder affected the redistribution of turbulent kinetic energy (TKE) before impact, leading to a decrease in TKE and Reynolds stresses in the inner part of the current's head. Finally, Brito et al. [44] used velocity and density measurements in the same configuration as in Di Lollo et al. [43] to validate a LES model. The three papers mentioned above analysed the dynamics of the interaction between a gravity current and an isolated cylinder without varying the height or diameter of the obstacle. Furthermore, there are no studies on the changes induced by the presence of an isolated cylinder on the mixing processes. In this study, measurements of the instantaneous density fields are used to investigate the effects of the presence of a single cylinder on the propagation, anatomy and mixing of a gravity current as the Reynolds number, the height and the diameter of the obstacle are varied. The paper is structured as follows: Sect. 2 describes the experimental setup and methodology. Section 3 presents the results obtained from the experiments, such as the evolution and the velocity of the gravity current front , the depth-averaged density fields, a quantitative assessment of the entrainment processes, and a discussion of the energy budgets. Finally, Sect. 4 summarises the main conclusions.

2 Experimental details

2.1 Experimental set-up

Experiments are conducted at the Hydraulics Laboratory of Roma Tre University using a horizontal Perspex channel with dimensions of 3 m in length, 0.4 m in height, and 0.2 m in width. The channel is divided into two volumes by a gate positioned at $x_0 = 0.3$ m from the left side of the channel (Fig. 1). The dense fluid , with density ρ_d, is added to the lock volume, while the rest of the channel is filled with fresh water with density $\rho_a < \rho_d$. The two volumes are filled to have the same initial water depth $h_0 = 0.2$ m, so gravity currents are generated in the full-depth lock-release condition.

The amount of salt added in the lock is varied in the experiments to achieve two different reduced gravities, $g' = g\frac{\rho_d - \rho_a}{\rho_a}$, equal to $g' = 0.06$ m s^{-2} and $g' = 0.24$ m s^{-2}. The initial density in each experiment is measured using an electronic density meter (Anton Paar DMA 4100 M) with an accuracy of 10^{-4} g cm^{-3}. An isolated obstacle was simulated by placing a single vertical cylinder on the bottom. The cylinder is positioned at a distance of 2 x_o from

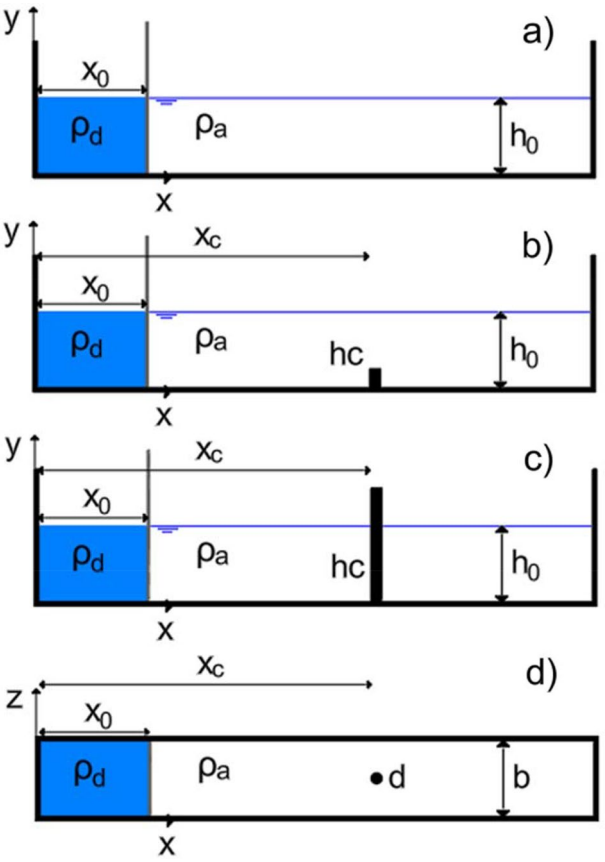

Fig. 1 Side view of the experimental setup for: **a** undisturbed configuration (no obstacle); configurations with the obstacle with $d = 3$ cm and **b** submergence ratio $h_0/h_c = 4$ and **c** submergence ratio $h_0/h_c = 1$. **d** Top view for the configuration with the obstacle with $d = 3$ cm

the lock, at half width of the channel. Three different cylinder diameters d =3 cm, 5 cm and 9 cm are tested to analyse the impact of different flow blockage ratios defined as b/d, where b is the channel width (0.2 m). For each diameter, three different cylinder heights h_c = 5 cm, 10 cm and 30 cm are examined to analyse the effect of the different submergence ratios h_0/h_c. In particular, two submerged cylinders ($h_0/h_c > 1$) and one emergent cylinder ($h_0/h_c = 1$) are analysed (Fig. 1).

The experiment begins with the removal of the gate and the consequent collapse of the dense fluid, which starts to propagate along the bottom towards the right side of the channel. The experiment ends when the current reaches the end of the channel. A camera (Sony RX100 IV) with a resolution of 2523 x 255 pixels, positioned perpendicular to the channel and aligned at its center, records the experiment at a frequency of 25 Hz, framing the entire length of the domain with an accuracy of $\sim$ 1 mm pixel^{-1}. A custom-made panel of LED lights with a diffuser screen ensures uniform back-lighting across the entire channel. A total of 20 experiments have been performed and are summarized in Table 1. 2 experiments have been conducted on a smooth bed (prefix S) and 18 experiments have been conducted with the cylinder (prefix C). The initial Reynolds number Re_0 is defined as [2]:

Table 1 Summary of the initial parameters characterizing the experiments

Run	g' [m/s^2]	Re_0	b/d	h_0/h_c	Marker
S1	0.06	1.1×10^4	–	–	
S2	0.24	2.2×10^4	–	–	○
C1	0.06	1.1×10^4	6.67	4	
C2	0.06	1.1×10^4	6.67	2	
C3	0.06	1.1×10^4	6.67	1	
C4	0.06	1.1×10^4	4	4	
C5	0.06	1.1×10^4	4	2	
C6	0.06	1.1×10^4	4	1	
C7	0.06	1.1×10^4	2.2	4	
C8	0.06	1.1×10^4	2.2	2	
C9	0.06	1.1×10^4	2.2	1	
C10	0.24	2.2×10^4	6.67	4	■
C11	0.24	2.2×10^4	6.67	2	■
C12	0.24	2.2×10^4	6.67	1	■
C13	0.24	2.2×10^4	4	4	▲
C14	0.24	2.2×10^4	4	2	▲
C15	0.24	2.2×10^4	4	1	▲
C16	0.24	2.2×10^4	2.2	4	◆
C17	0.24	2.2×10^4	2.2	2	◆
C18	0.24	2.2×10^4	2.2	1	◆

$$Re_0 = \frac{u_b h_0/2}{\nu} \tag{1}$$

where $u_b = \sqrt{g' h_0}$ is the buoyancy velocity and ν is the kinematic viscosity.

2.2 Density measurements

The instantaneous density field is measured by an image analysis using a light attenuation technique, that relates light intensity to the known concentration of a dye (methylene blue) added to the lock, following the approach described in Adduce et al. [34]. The method relies on pixel-based calibration using nine images: the first corresponds to zero dye concentration (ambient fluid), while increasing amounts of dye are added in the subsequent eight images to reach the concentration used in the lock. A calibration curve for each pixel is generated by a non-linear interpolation of these nine images. The density field is then determined by assuming a linear relationship between the dye concentration and the salt concentration. For a more detailed explanation of the technique used,please refer to Adduce et al. [34]. The instantaneous dimensionless density field $\rho^*(x, y, t)$ is defined as :

$$\rho^*(x, y, t) = \frac{\rho(x, y, t) - \rho_a}{\rho_d - \rho_a} \tag{2}$$

3 Results

3.1 Current evolution

The variations induced by the presence of a vertical obstacle on the dynamics of a gravity current are highlighted through the analysis of the instantaneous dimensionless density field ρ^*. Figure 2 shows the evolution of the dimensionless spanwise-averaged density field, ρ^*, at different stages of the flow evolution for the undisturbed run (S2, panels a, b, and g), as well as for runs with flow blockage ratios $b/d = 2.2$ and submergence ratios $h_0/h_c = 4$ (C16, panels c, d, and h) and $h_0/h_c = 1$ (C18, panels e, f, and i). The frames correspond to travel distances equal to $x^* = (x - x_0)/x_0 = 1.93$ (panels a, c and e), $x^* = 3$ (panels b,d, and f) and $x^* = 8.67$ (panels g,h,i). The dimensionless vertical coordinate is evaluated as $y^* = y/h_0$. Before the impact, configurations with the cylinder do not exhibit any appreciable differences compared to the undisturbed run (S2), in agreement with Di Lollo et al.

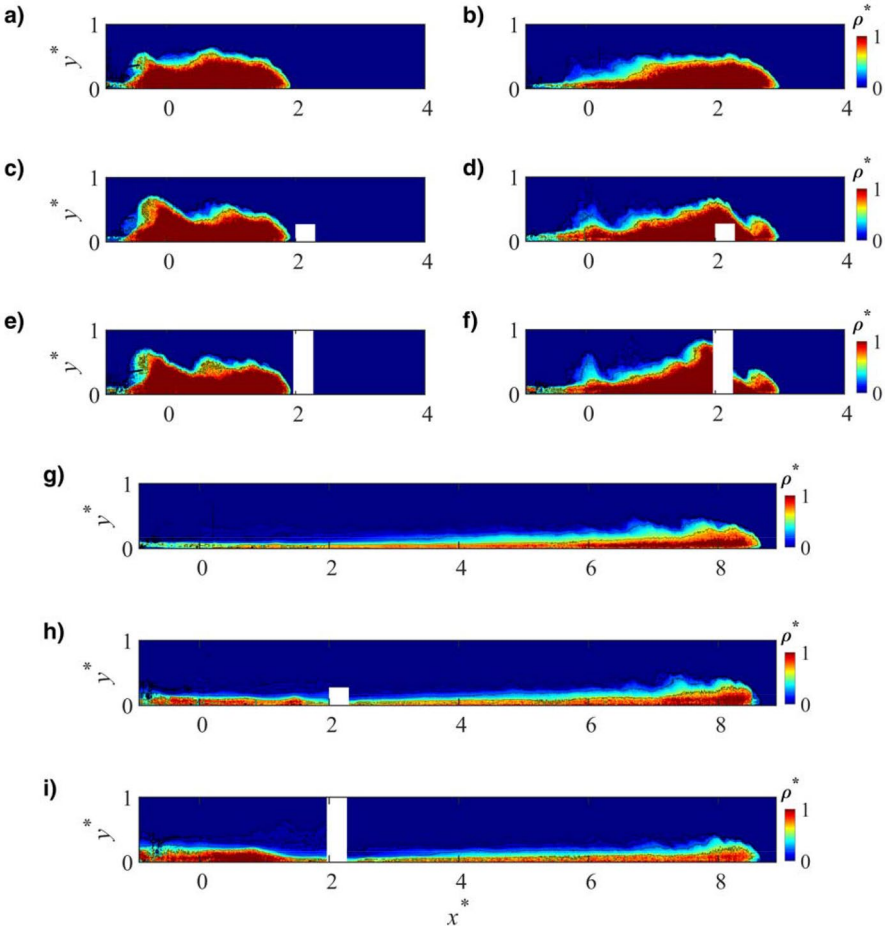

Fig. 2 Propagation of the current for the runs: S2 **a**, **b** and **g**; C16 **c**, **d** and **h**; C18 **e**, **f** and **i**. The frames correspond to travel distances $x^* = 1.93$ **a**, **c** and **e**, $x^* = 3$ **b**, **d**, and **f**, and $x^* = 8.67$ panels **g**, **h**, **i**

[43]. Indeed, in all cases, the flow exhibits a well-defined head followed by a trailing body (Fig. 2a, c, and e).The run S2 shows this behaviour for the whole experiment, showing a decrease in density and an increase in volume, due to the entrainment of ambient fluid and the consequent mixing between the two fluids (Fig. 2b, g). In the run C16 part of the current flows along the sides of the cylinder, with a reduced thickness compared to the upstream region. Another portion of the flow is deflected upwards in front of the obstacle and then passes over it, leading to a local thinning of the flow downstream of the cylinder (Fig. 2 d). A similar behavior has been observed in the run C18, which shows that the presence of an obstacle occupying the whole height of the ambient fluid has a significant impact on the current propagation. The current depression over the obstacle is more pronounced, and the flow rises to a larger height upstream of the cylinder. After the passage of the current, there is the formation of a larger interface vortex immediately downstream of the cylinder (Fig. 2 f). By the end of the experiment, the currents interacting with the cylinder are more diluted than the undisturbed run. In addition, due to the presence of an obstacle, part of the current is reflected and returns toward to the left end of the channel. The higher the obstacle, the larger the dilution and reflection of the current (Fig. 2h, i).

3.2 Front characteristics

The front position x_f is defined as the streamwise coordinate of the foremost point of the dense current. The dimensionless front position x_f^* is given by:

$$x_f^* = \frac{x_f - x_0}{x_0} \tag{3}$$

The evaluation of the front position is obtained by adopting a density threshold of 2%, i.e. $\rho^* = 0.02$ [34]. In the lock-exchange configuration, the propagation of the gravity current develops three distinct phases [4, 7]. Immediately after the gate removal, a rapid collapse occurs, generating a dense bottom current. During this initial slumping phase, the front advances at an approximately constant velocity, resulting in a linear increase in the front position. The flow then enters the self-similar (or inertial–buoyancy) phase, initiated when the bore of the ambient fluid reflected by the left-side wall overtakes the front of the gravity current [1, 4, 45, 46]. In this regime, the front velocity decreases with time as $t^{(-1/3)}$, while the front position grows as $t^{(2/3)}$, where t is the time elapsed since gate removal. Finally, when viscous forces become dominant over inertial effects, the current transitions into the viscous–buoyancy phase, characterized by a front velocity scaling as $t^{(-4/5)}$ and front position advancing as $t^{(1/5)}$ [3].

Figure 3 shows dimensionless front position x_f^* versus dimensionless time t^* , defined as $t^* = t/(x_0/\sqrt{g'h_0})$. The results are presented for runs with $g' = 0.24$ m s^{-2} and flow blockage ratios $b/d =$ 6,67, (Fig. 3a) and $b/d =$ 2,2 (Fig. 3b). A comparison of the flow behavior between all three blockage ratios for the runs with submergence ratios $h_0/h_c = 1$ is shown in Fig. 3c. Runs in the undisturbed configuration are developed entirely in the slumping phase. This is in agreement with the literature since the transition between the slumping phase and the self similar phase has been shown to occur for $x_f^* \sim 9$ [23, 45]. In runs with obstacles, the front propagation can be approximated by a linear law. Previous studies on gravity currents interacting with an isolated obstacle occupying the entire width

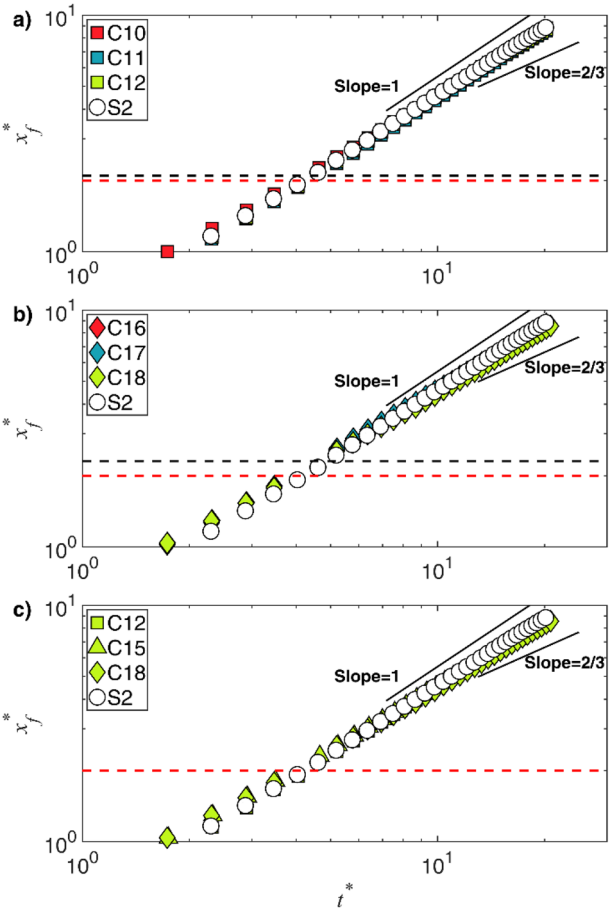

Fig. 3 x_f^* versus t^* for all the runs with $g' = 0.24$ m s^{-2} and **a** $b/d = 6{,}67$, **b** $b/d = 2{,}2$ and **c** $h_0/h_c = 1$. Red dashed lines represent the onset of the cylinder while black dashed lines represent the end of the cylinder. The black lines represent the slumping phase (slope 1) and self-similar phase (slope 2/3)

of the channel [36] or with a bottom roughness [22, 23, 29] have identified the transition from the slumping phase to the self-similar phase. Instead, the presence of a single vertical cylinder does not cause the transition to the self-similar phase, regardless of its height and diameter. No differences have been found for the runs characterised by $g' = 0.06$ m s^{-2}.

The front velocity is evaluated as $U_f = \Delta x_f/\Delta t = (x_f(t) - x_f(t_0))/(t - t_0)$, where t_0 is the time of the gate removal. The dimensionless value U_f^* is obtained as follows:

$$U_f^* = \frac{U_f}{u_b} \tag{4}$$

Figure 4 shows the evolution of the dimensionless front velocity versus the dimensionless front position for the runs characterized by $g' = 0.24$ m s^{-2} and flow blockage ratios $b/d = 6{,}67$, (Fig. 4a) and $b/d = 2{,}2$ (Fig. 4b) . A comparison of the effects of emergent obstacles for all three blockage ratios is presented in Fig. 4c. The undisturbed configuration shows a constant front velocity for all its development, confirming that its propagation takes place in the slumping phase, in both the reduced gravities tested. In the undisturbed run with reduced gravity $g' = 0.24$ m s^{-2} (white circles in Fig. 4), the front propagates with $U_f^* \sim 0.44$, for

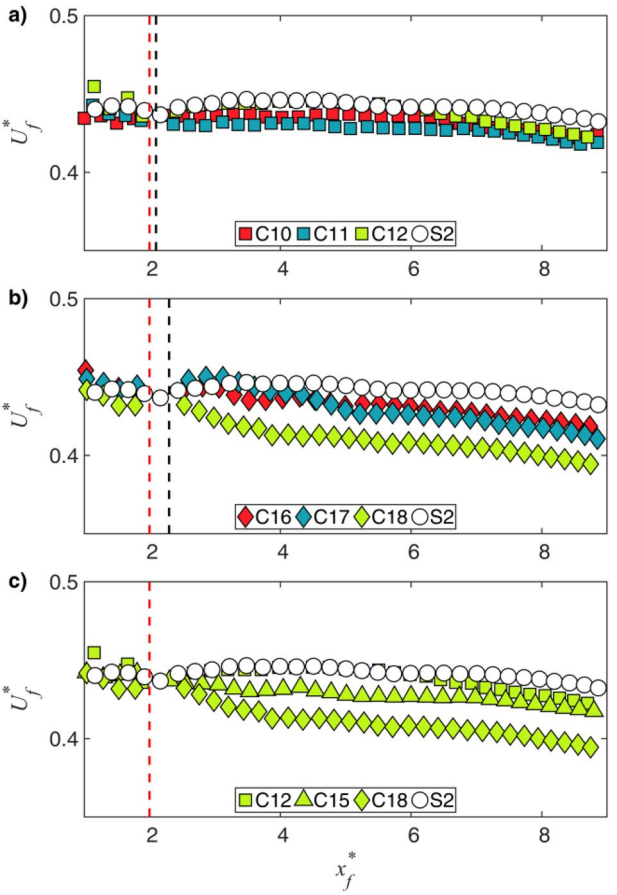

Fig. 4 U_f^* versus x_f^* for all the runs with $g' = 0.24$ m s^{-2} and **a** $b/d = 6{,}67$, **b** $b/d = 2{,}2$ and **c** $h_0/h_c = 1$. Red dashed lines represent the onset of the cylinder while black dashed lines represent the end of the cylinder

the one with $g' = 0.06$ m s^{-2} with $U_f^* \sim 0.43$ (not shown), in agreement with the previous studies' findings that $0.4 < U_f^* < 0.5$ [5, 24, 47–49]. In the experiments with obstacles, the front velocity remains constant before impact, following a pattern similar to the undisturbed run for all tested configurations. This differs from the observations of a submerged obstacle spanning the entire domain width, where front deceleration occurred before impact [50, 51]. Fig. 4a shows that for a flow blockage ratio $b/d = 6{,}67$, the front decelerates slightly. At the end of the test, all the configurations with $b/d = 6{,}67$ show an equal difference in front velocity compared to the undisturbed configuration, indicating that U_f^* is not affected by the degree of submergence of the obstacle for this flow blockage ratio. A similar trend has been observed for $b/d = 4$ (not shown). The deceleration induced by the presence of a cylinder is more pronounced in the case of $b/d = 2.2$ (Fig. 4b). Submerged obstacles show a similar trend in U_f^*. The slowdown starts for $x_f^* \sim 3.5$ and U_f^* shows approximately equal values for the two submergence ratios. In the case of an emergent obstacle, deceleration starts immediately downstream of the cylinder and U_f^* has lower values than for submerged obstacles, settling at a final value of $U_f^* \sim 0.395$. The distance from the cylinder at which the front begins to decelerate decreases as the cylinder diameter increases, as shown in Fig. 4c. U_f^* shows similar values at the end of the experiment for the flow blockage ratios

$b/d = 6{,}67$ and $b/d = 4$. This indicates a negligible difference in the propagation of the front between the flow blockage ratios $b/d = 6{,}67$ and $b/d = 4$. The run C18 shows a deceleration larger than the smaller diameter configurations with the same submergence ratio.

3.3 Depth-averaged density fields and current thickness

The main features of gravity currents dynamics can be derived from the analysis of the depth-averaged density ρ_v, which is obtained by integrating the instantaneous density field ρ^*, below its upper boundary; the latter is defined by a threshold of dimensioless density of 2%. The dimensionless depth-averaged density ρ_v^* is defined as:

$$\rho_v^*(x,t) = \frac{\rho_v - \rho_a}{\rho_d - \rho_a} \tag{5}$$

The space-time evolutions of the dimensionless depth-averaged density fields ρ_v^* is shown in Fig. 5 for the runs characterized by $g' = 0.24$ m s^{-2}. Fig. 5 shows the Hovmöller diagrams of ρ_v^* in the $x^* - t^*$ plane for the undisturbed run (S2, panel a), for all the runs with flow blockage ratio $b/d = 2{,}2$ (C16, C17, C18, panels b,c,d, respectively) and for the runs with submergence ratio $h_0/h_c = 1$ and flow blockage ratios $b/d = 6.67$ (C12, panel e) and $b/d = 4$ (C15, panel f). The separation between the white area and the color-map represents the current front which propagates with a linear variation in time for all the configurations. In configurations with cylinders, the current exhibits lower values of ρ_v^* all over the area downstream of the cylinder compared to the undisturbed case. This implies a larger dilution of the current in the presence of an obstacle, which increases as the obstacle height increases. Downstream of the cylinder, at $x^* \sim 3$, the current shows a local dilution larger than in the undisturbed case, which also increases as the height of the obstacle increases

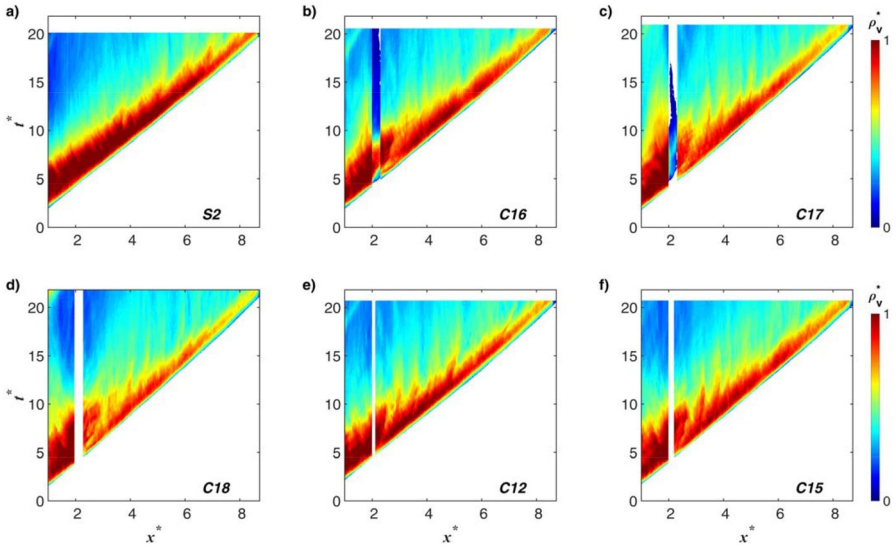

Fig. 5 Dimensionless depth-averaged density fields ρ_v^* of the current for the runs **a** S2; **b** C16; **c** C17; **d** C18; **e** C12 and **f** C15

(Fig. 5b,c and d). Focusing on the area occupied by the cylinder ($2 < x^* < 2.3$ in Fig. 5b,c and d), the current overflows the obstacle for the whole duration of the experiment in run C16 (Fig. 5b), only partially in run C17 (Fig. 5c), and never in run C18 (Fig. 5d). The dilution downstream of the cylinder increases as the cylinder diameter increases for the same submergence ratio, as can be seen from the comparison of the Hovmöller diagrams shown in Fig. 5d,e and f.

The current thickness $h(x, t)$ is evaluated as the interface between the dense and light fluids by considering as upper boundary the iso-density threshold 2%. The space-time evolution of the dimensionless current thickness, $H^* = h(x,t)/h_0$, is shown in Fig. 6 for the same experimental runs of Fig. 5. The presence of an obstacle substantially changes H^* compared to the undisturbed run. In each configuration with the cylinder, upstream of it there is an increase of H^*, the larger is the height of the obstacle the larger is H^*. Similarly, the current thickness decreases downstream of the obstacle, the larger is the height of the obstacle the lower is the current thickness downstream of the obstacle. In the run C16 (Fig. 6b), the current thickness is larger than the height of the obstacle for the whole duration of the experiment, whereas in the run C17 (Fig. 6c) the current thickness is larger than the obstacle height only for a short time. The increase in H^* upstream of the cylinder and the decrease downstream of the obstacle become more evident as the obstacle diameter increases for the same submergence ratio, as can be seen from the comparison of the Hovmöller diagrams shown in Fig. 6d,e and f.

3.4 Entrainment

During its propagation the dense current entrains ambient fluid increasing its volume. This mixing process can be parameterized by the dimensionless velocity at which the ambient fluid crosses the interface with the dense fluid, known as the bulk entrainment parameter E_{bulk} [24, 52]. Given the initial volume V_0 of the gravity current at $t_0 = 0$, at a later time

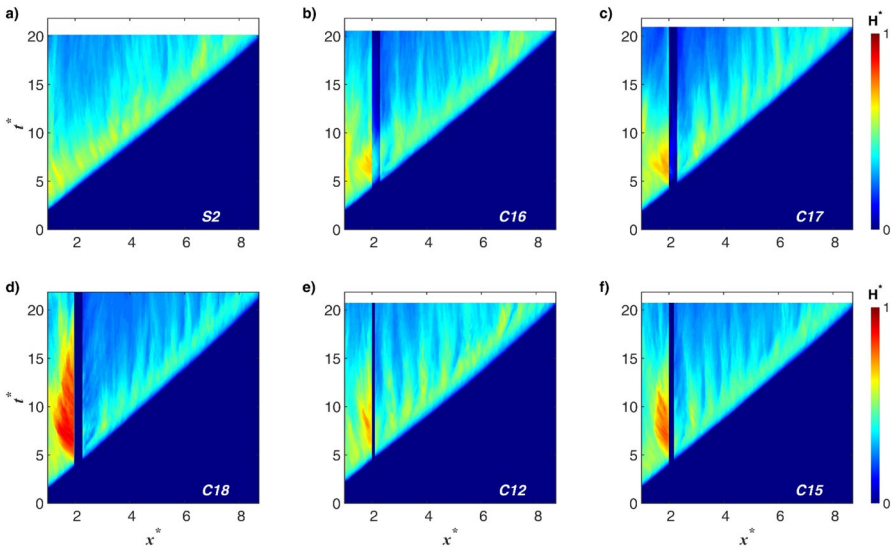

Fig. 6 Dimensionless current thickness for runs **a** S2; **b** C16; **c** C17; **d** C18; **e** C12 and **f** C15

$t_i = t_0 + \Delta t_i$, the dense current will have a larger volume $V_i = V_0 + \Delta V_i$, where ΔV_i can be determined by:

$$\Delta V_i = (A_i - A_0)b \tag{6}$$

A_i and A_0 are the current areas respectively at t_i and t_0 and b is the width of the channel. A bulk entrainment velocity, $W_{e,i}$ can be defined by

$$W_{e,i} = \frac{Q_{e,i}}{S_i} \tag{7}$$

where $Q_{e,i} = \Delta V_i/(t_i - t_0)$ is the entrainment discharge and S_i is the interface separating the two fluids, which can be evaluated as the product between the width of the channel and the front position at t_i. Finally, the bulk entrainment parameter $E_{bulk,i}$ is evaluated as [46]:

$$E_{bulk,i} = \frac{W_{e,i}}{2U_{f,i}} \tag{8}$$

Fig. 7a shows the entrainment parameter E_{bulk} versus x_f^* for runs with $g' = 0.24$ m s^{-2} and flow blockage ratios $b/d = 2{,}2$. The entrainment parameter has an order of magnitude of 10^{-2} and decreases with the distance travelled by the current, in agreement with the literature [7, 24]. The presence of a vertical cylinder does not affect the entrainment parameter. Similar results have been found for all the configurations tested. Figure 7b and c show E_{bulk} as a function of the bulk Reynolds number, *Re* and Froude number *Fr*, respectively, evaluated at $x_f^* = 8$ for all the runs characterized by $g' = 0.24$ m s^{-2}. These numbers are defined as [5, 29]:

$$Re = \frac{U_f h_0/2}{\nu} \tag{9}$$

$$Fr = \frac{U_f}{\sqrt{g'_m h_0/2}} \tag{10}$$

where g'_m is the bulk reduced gravity. There is no appreciable change in E_{bulk} depending on the bulk Reynolds and Froude numbers tested. Same results have been found for all the runs characterized by $g' = 0.06$ m s^{-2} (not shown). We can therefore conclude that the presence of a vertical cylinder of different height or diameter does not affect the entrainment parameter of a gravity current. Fig. 7d and e show E_{bulk} versus the flow blockage ratios b/d and the submergence ratio h_0/h_c for all the runs with $g' = 0.24$ m s^{-2}, respectively. There is no appreciable change of E_{bulk} parameter depending on b/d and h_0/h_c.

3.5 Energy budget and irreversible mixing

The entrainment parameter depends on the isodensity chosen to define the interface between the dense current and ambient fluid. The energy budget method allows to have evaluations of the mixing process not dependent on the choice of an isodensity threshold. This method

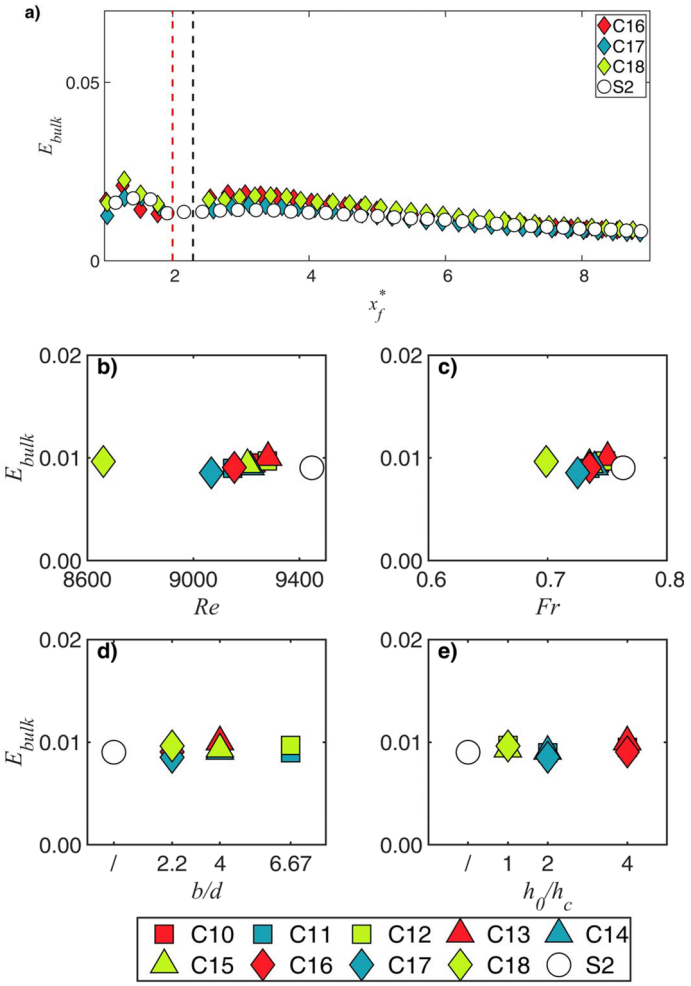

Fig. 7 **a** E_{bulk} versus x_f^* for all the runs with $g' = 0.24$ m s^{-2} and $b/d = 2{,}2$. Red dashed lines represent the onset of the cylinder while black dashed lines represent the end of the cylinder; E_{bulk} as a function of the bulk Reynolds number, *Re* and Froude number *Fr* for all the runs $g' = 0.24$ m s^{-2} **b** and **c**, respectively); **d** E_{bulk} versus *b*/*d* and **e** E_{bulk} versus $h_0/h_c =$ for all the runs with $g' = 0.24$ m s^{-2}

separates the changes in potential energy induced by adiabatic processes, which modify potential energy without mass or heat exchange, from those caused by diabatic processes, which are associated to irreversible mixing [53, 54]. The potential energy, $E_p(t)$, of a gravity current is defined as:

$$E_p(t) = g \int_V \rho(x, y, t) y \, dV. \tag{11}$$

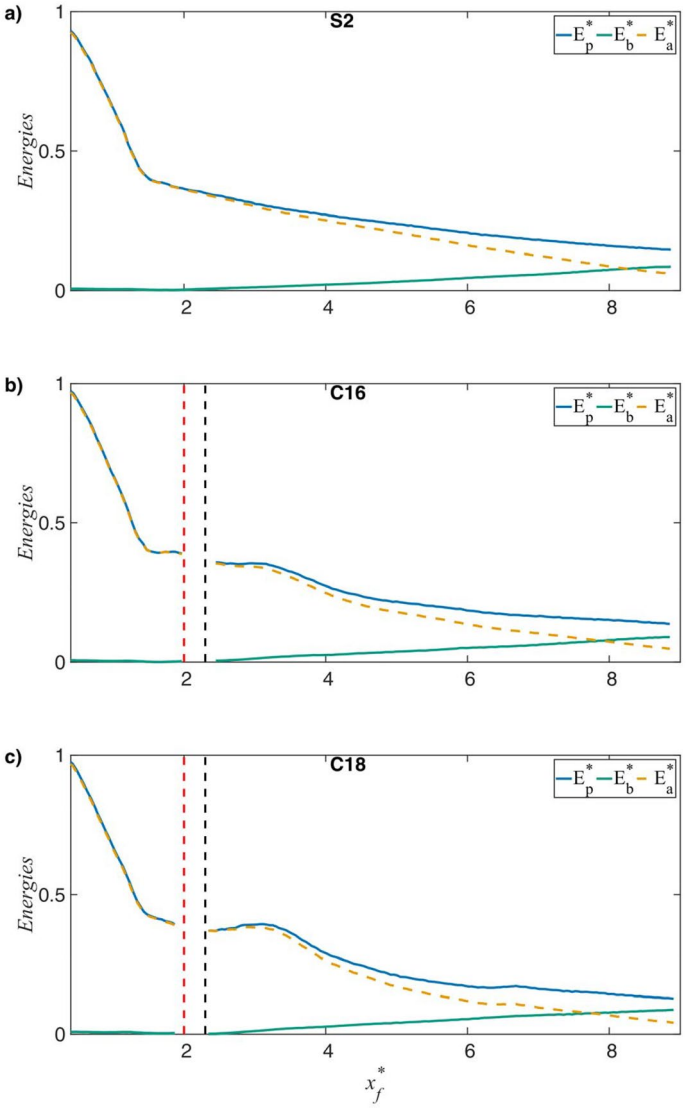

Fig. 8 Energy budget versus x_f^* for the runs **a** S2; **b** C16 and **c** C18. Red dashed lines represent the onset of the cylinder while black dashed lines represent the end of the cylinder

where $\rho(x, y, t)$ is the instantaneous density field and V is the entire volume of the domain, i.e. the sum of the dense and ambient fluid volumes. The background potential energy E_b is defined as:

$$E_b(t) = g \int_V \tilde{\rho}(x, y, t) y \, dV. \tag{12}$$

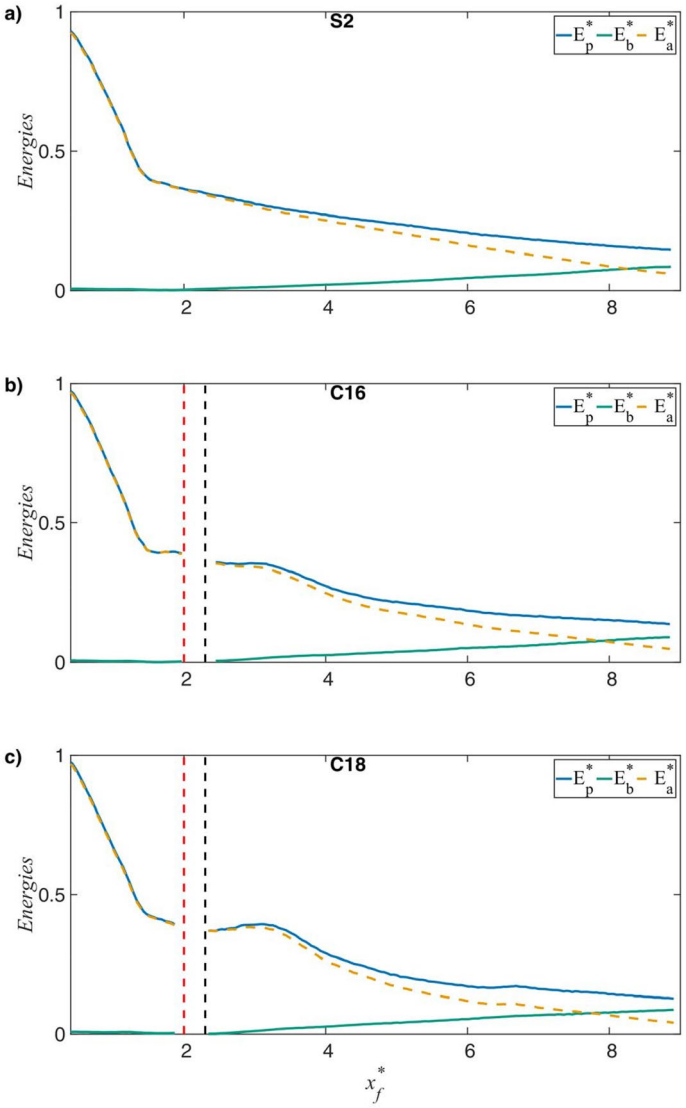

Fig. 9 Energy budget versus x_f^* for **a** C12; **b** C15 and **c** C18. Red dashed lines represent the onset of the cylinder while black dashed lines represent the end of the cylinder

where $\tilde{\rho}(x, y, t)$ is the density field rearranged by placing the particles in a stable stratification, to obtain the minimum potential energy configuration. Changes in $E_b(t)$ are associated to irreversible mixing. Finally, the available potential energy E_a is the part of potential energy which can be converted into kinetic energy [34]. In an isolated system, E_a is defined as:

$$E_a(t) = E_p(t) - E_b(t) \tag{13}$$

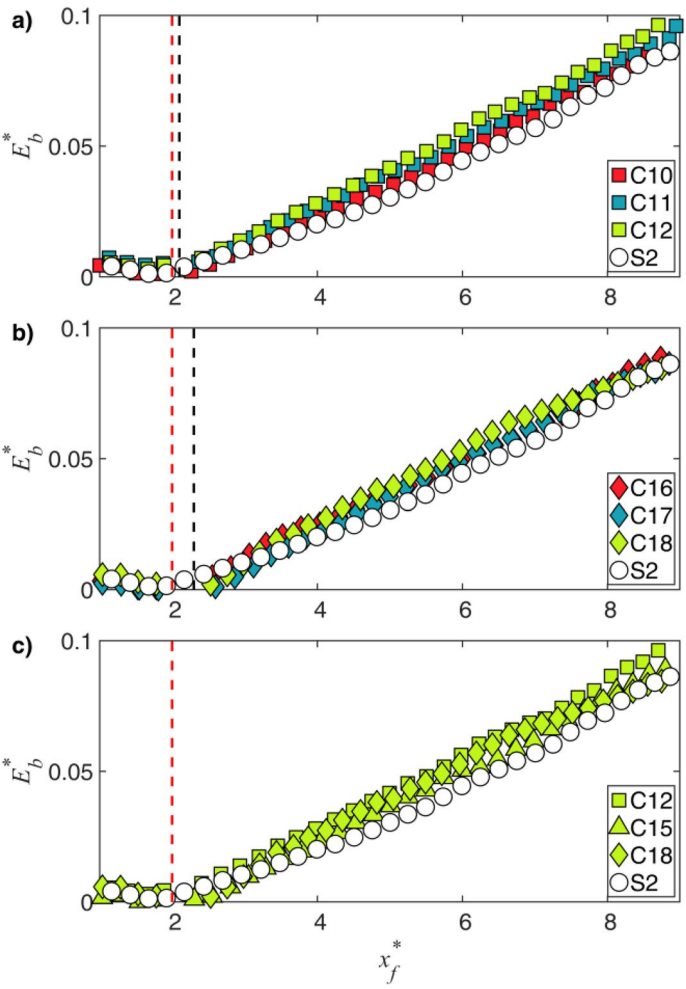

Fig. 10 Dimensionless background potentional energy versus x_f^* for all the runs with $g' = 0.24$ m s^{-2} and **a** $b/d = 6{,}67$, **b** $b/d = 2{,}2$ and **c** $h_0/h_c = 1$. Red dashed lines represent the onset of the cylinder while black dashed lines represent the end of the cylinder

The dimensionless energies E_p^*, E_b^*, and E_a^* are defined so that the minimum of E_b^* at the initial time is zero, and the maximum of E_p^* at $t = 0$ is equal to 1.

Figure 8 shows the energy budget versus x_f^* for runs with $g' = 0.24$ m s^{-2} characterized by a flow blockage ratio $b/d = 2.2$, while Fig. 9 compares the energy budget for the runs with $g' = 0.24$ m s^{-2} in presence of the emergent cylinder. No appreciable differences have been found with runs with $g' = 0.06$ m s^{-2}. E_p^* for S2 (Fig. 8a) decreases as the distance traveled by the current increases and its behavior agrees with the literature [53, 54]. For the run C16 (Fig. 8b) a slight increase in the values of E_p^* is present when $x_f^* \sim 3$, due to an increase in the thickness of the current after the interaction with the obstacle. These increase in E_p^* is more evident for the run C18 (Fig. 8c), due to an higher increase in thickness in presence of the emergent cylinder. The increase in E_p^* is not evident for the runs C12

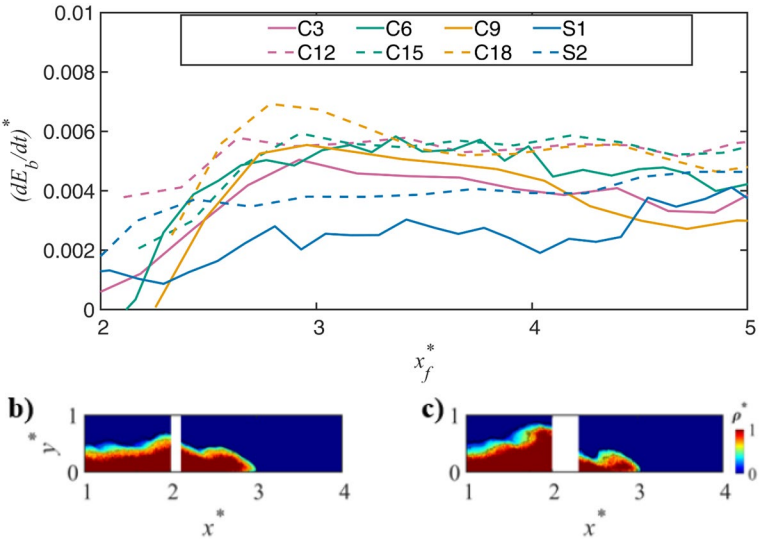

Fig. 11 **a** $(dE_b/dt)^*$ versus x_f^* for the runs S1, C3, C6, C9, S2, C12, C15 and C18. Solid lines represent runs characterized by $g' = 0.06$ m s^{-2}, dashed lines represent runs characterized by $g' = 0.24$ m s^{-2} . Evolution of the flow in the runs **b** C12 and **c** C18 when $x_f^* = 3$

(Fig. 9a) and C15 (Fig. 9b) configurations. Significant variations of E_p^* compared to the undisturbed case are therefore only present for a flow blockage ratio equal to $b/d = 2.2$. E_b^* increases as the distance traveled by the current increases due to the presence of irreversible mixing for all the configurations tested.

Figure 10 shows the background potential energy E_b versus x_f^* for the runs with $g' = 0.24$ m s^{-2} and flow blockage ratios $b/d = 6{,}67$, (Fig. 10a) and $b/d = 2{,}2$ (Fig. 10b) and a comparison between the emergent obstacles for the three flow blockage ratios (Fig. 10c). The behavior of E_b^* before the current nose reaches the obstacle ($x_f^* < 2$) does not vary compared to the undisturbed case. The configuration characterized by a flow blockage ratio of $b/d = 6.67$ (Fig. 10a) shows a higher growth rate of E_b^* when $2 < x_f^* < 5$ compared to the undisturbed configuration, showing an increase in irreversible mixing. The growth rate increases with increasing cylinder height (Fig. 10a and b) and diameters(Fig. 10c). No significant differences have been observed for the runs with $g' = 0.06$ m s^{-2}.

Figure 11a compares $(dE_b/dt)^*$ versus x_f^* for the runs S1, C3, C6, C9, S2, C12, C15 and C18, after the front has traveled a distance $2 < x_f^* < 5$, the region where the maximum slope of E_b^* versus x_f^* has been identified in Fig. 10. The configurations with the cylinder show an increase of $(dE_b/dt)^*$ compared to the undisturbed case, for both the reduced gravities tested. The maximum increase occurs for run C18 for $2.5 < x_f^* < 3.5$. The increase of $(dE_b/dt)^*$ shows an increase of irreversible mixing processes compared to the undisturbed case, due to the development of an instability caused by the interaction with the cylinder. The increase of mixing is due to the increase of the flow thickness upstream of the obstacle and the formation of a vortex following the drop downstream of the cylinder. These mechanisms are more evident as the diameter of the cylinder increases, as shown in Fig. 11b and c, which show the evolution of the flow in the runs C12 and C18 when $x_f^* = 3$, respectively.

4 Conclusions

This paper studies the influence of an isolated cylinder on the dynamics of gravity currents generated by a lock release. The analyses are carried out by measurements of the instantaneous density field obtained through a light attenuation technique based on nine calibration images. Two reduced gravities are tested to study the effects on a different Reynolds's number. Three cylinder heights and three diameters are used to analyse the effects of different degrees of submergence and flow blockage ratios on the dynamics of a gravity current. Upstream of the cylinders, there are no substantial differences in the current propagation in each tested configuration. The front velocity slows down downstream of the cylinder compared to the undisturbed case and the deceleration increases as the diameter of the obstacle increases. The deceleration is not significantly affected by the Reynolds number or the different degrees of submergence. The deceleration of the front does not cause the transition from the slumping phase to the self-similar phase. The major influence of the different degree of submergence lies in a larger increase of the current's thickness following the impact upstream of the cylinders, the larger is the height of the obstacle the larger is thickness of the current. A larger diameter of the obstacle causes a larger increase of the thickness of the current and a larger reflection of the dense current upstream of the obstacle. The tested obstacles, of any degree of submergence and flow blockage ratio, do not cause substantial variations in the entrainment parameter. The energy budget method shows a slight increase in the mixing process in presence of an obstacle compared to the undisturbed case. A larger diameter and a larger height of the cylinder causes larger variation in the irreversible mixing processes and larger dilution of the current at the end of the experiments.

Acknowledgements This research was funded by European Union - Next Generation EU, Mission 4, Component 1 CUP F53D23001910006.

Author contributions These authors contributed equally to this work

Funding Open access funding provided by Università degli Studi Roma Tre within the CRUI-CARE Agreement.

Data availability Data will be made available on request.

Declarations

Conflict of interest The authors declare that they have no known competing financial interests or personal relationships that could have appeared to influence the work reported in this paper.

References

1. Simpson JE (1999) Gravity currents: in the environment and the laboratory. Cambridge University Press, Cambridge
2. Benjamin TB (1968) Gravity currents and related phenomena. J Fluid Mech 31(2):209–248
3. Huppert HE, Simpson JE (1980) The slumping of gravity currents. J Fluid Mech 99(4):785–799
4. Huppert HE (1982) The propagation of two-dimensional and axisymmetric viscous gravity currents over a rigid horizontal surface. J Fluid Mech 121:43–58
5. Marino B, Thomas L, Linden P (2005) The front condition for gravity currents. J Fluid Mech 536:49–78
6. Zhu JB, Lee CB, Chen GQ, Lee JHW (2006) Piv observation of instantaneous velocity structure of lock release gravity currents in the slumping phase. Commun Nonlinear Sci Numer Simul 11(2):262–270
7. Adduce C, Sciortino G, Proietti S (2012) Gravity currents produced by lock exchanges: experiments and simulations with a two-layer shallow-water model with entrainment. J Hydraul Eng 138(2):111–121
8. Zordan J, Juez C, Schleiss AJ, Franca MJ (2018) Entrainment, transport and deposition of sediment by saline gravity currents. Adv Water Resour 115:17–32
9. Zordan J, Schleiss A, Franca M (2018) Structure of a dense release produced by varying initial conditions. Environ Fluid Mech 18(5):1101–1119
10. De Falco MC, Adduce C, Cuthbertson A, Negretti ME, Laanearu J, Malcangio D, Sommeria J (2021) Experimental study of uni-and bi-directional exchange flows in a large-scale rotating trapezoidal channel. Phys Fluids 33(3):036602
11. Dai A, Huang Y-L (2024) The flow within the head of a gravity current. J Fluid Mech 997:42
12. Cuthbertson A, Lundberg P, Davies P, Laanearu J (2014) Gravity currents in rotating, wedge-shaped, adverse channels. Environ Fluid Mech 14:1251–1273
13. Laanearu J, Cuthbertson AJ, Davies PA (2014) Dynamics of dense gravity currents and mixing in an up-sloping and converging vee-shaped channel. J Hydraul Res 52(1):67–80
14. Negretti M-E, Flor J-B, Hopfinger EJ (2017) Development of gravity currents on rapidly changing slopes. J Fluid Mech 833:70–97
15. Martin A, Negretti ME, Hopfinger EJ (2019) Development of gravity currents on slopes under different interfacial instability conditions. J Fluid Mech 880:180–208
16. De Falco M, Ottolenghi L, Adduce C (2020) Dynamics of gravity currents flowing up a slope and implications for entrainment. J Hydraul Eng 146(4):04020011
17. De Falco M, Adduce C, Negretti M, Hopfinger E (2021) On the dynamics of quasi-steady gravity currents flowing up a slope. Adv Water Resour 147:103791
18. Dai A, Huang Y-L (2020) Experiments on gravity currents propagating on unbounded uniform slopes. Environ Fluid Mech 20(6):1637–1662
19. Dai A, Huang Y-L (2021) Boussinesq and non-boussinesq gravity currents propagating on unbounded uniform slopes in the deceleration phase. J Fluid Mech 917:23
20. Maggi M, Adduce C, Lane-Serff G (2023) Gravity currents interacting with slopes and overhangs. Adv Water Resour 171:104339
21. La Rocca M, Adduce C, Sciortino G, Pinzon AB (2008) Experimental and numerical simulation of three-dimensional gravity currents on smooth and rough bottom. Phys Fluids 20(10)
22. Tokyay T, Constantinescu G, Gonzalez-Juez E, Meiburg E (2011) Gravity currents propagating over periodic arrays of blunt obstacles: effect of the obstacle size. J Fluids Struct 27(5–6):798–806
23. Nogueira HI, Adduce C, Alves E, Franca MJ (2013) Analysis of lock-exchange gravity currents over smooth and rough beds. J Hydraul Res 51(4):417–431
24. Nogueira HI, Adduce C, Alves E, Franca MJ (2014) Dynamics of the head of gravity currents. Environ Fluid Mech 14:519–540
25. Bhaganagar K, Pillalamarri NR (2017) Lock-exchange release density currents over three-dimensional regular roughness elements. J Fluid Mech 832:793–824
26. He Z, Han D, Lin YT, Zhu R, Yuan Y, Jiao P (2022) Propagation, mixing, and turbulence characteristics of saline and turbidity currents over rough and permeable/impermeable beds. Phys Fluids 34(6)
27. Maggi MR, Adduce C, Negretti ME (2022) Lock-release gravity currents propagating over roughness elements. Environ Fluid Mech 1–20
28. Maggi M, Hopfinger EJ, Sommeria J, Adduce C, Viboud S, Valran T, Negretti ME (2025) Laboratory experiments of rotating stratified exchange flows over a sediment bed. Adv Water Resour 200:104959
29. Maggi MR, Di Lollo G, Adduce C (2025) Dynamics and mixing of gravity currents over an array of cylindrical obstacles. Phys Fluids 37(7)
30. Lane-Serff G, Beal L, Hadfield T (1995) Gravity current flow over obstacles. J Fluid Mech 292:39–53
31. Gonzalez-Juez E, Meiburg E, Constantinescu G (2009) The interaction of a gravity current with a circular cylinder mounted above a wall: effect of the gap size. J Fluids Struct 25(4):629–640

32. Gonzalez-Juez E, Meiburg E, Tokyay T, Constantinescu G (2010) Gravity current flow past a circular cylinder: forces, wall shear stresses and implications for scour. J Fluid Mech 649:69–102
33. La Rocca M, Prestininzi P, Adduce C, Sciortino G, Hinkelmann R (2013) Lattice boltzmann simulation of 3d gravity currents around obstacles. Int J Offshore Polar Eng 23(03)
34. Adduce C, Maggi MR, De Falco MC (2022) Non-intrusive density measurements in gravity currents interacting with an obstacle. Acta Geophysica, 1–12
35. Wu CS, Ouyang HT (2020) Flow morphology in bottom-propagating gravity currents over immersed obstacles. AIP Adv 10(11)
36. De Falco M, Adduce C, Maggi M (2021) Gravity currents interacting with a bottom triangular obstacle and implications on entrainment. Adv Water Resour 154:103967
37. Laanearu J, Cuthbertson A (2023) Hydraulics of stratified sill flows within varying channel geometries: investigating energy loss and mixing of maximal two-layer exchange. Environ Fluid Mech 23(2):429–464
38. Maggi MR, Negretti ME, Hopfinger EJ, Adduce C (2023) Turbulence characteristics and mixing properties of gravity currents over complex topography. Phys Fluids 35(1)
39. Skevington EW, Hogg AJ (2023) The unsteady overtopping of barriers by gravity currents and dam-break flows. J Fluid Mech 960:27
40. Bardoel SL, Cheng S, Chamorro LP, Fernando HJ (2025) Gravity currents past thin two-dimensional obstacles. J Fluid Mech 1012:15
41. Maggi MR, Adduce C (2025) Laboratory experiments on reflected gravity currents and implications for mixing. Water 17(7):1062
42. Mok KM, Leong CS, Hoi KI, Yeh HH (2011)The impact of a gravity current with a vertically mounted circular cylinder: An experimental study. In: 2011 IEEE 3rd international conference on communication software and networks, pp. 194–198 . IEEE
43. Di Lollo G, Adduce C, Brito M, Ferreira RM, Ricardo AM (2024) Turbulent kinetic energy redistribution in a gravity current interacting with an emergent cylinder. Adv Water Resour 183:104585
44. Brito M, Ferreira R, Sousa A, Farias R, Di Lollo G, Ricardo A, Gil L (2022) Les validation of lock-exchange density currents interacting with an emergent bluff obstacle. Environ Fluid Mech 1–25
45. Rottman JW, Simpson JE (1983) Gravity currents produced by instantaneous releases of a heavy fluid in a rectangular channel. J Fluid Mech 135:95–110
46. Ottolenghi L, Adduce C, Inghilesi R, Armenio V, Roman F (2016) Entrainment and mixing in unsteady gravity currents. J Hydraul Res 54(5):541–557
47. Härtel C, Meiburg E, Necker F (2000) Analysis and direct numerical simulation of the flow at a gravity-current head. part 1. flow topology and front speed for slip and no-slip boundaries. J Fluid Mech 418, 189–212
48. Cantero MI, Lee JR, Balachandar S, Garcia MH (2007) On the front velocity of gravity currents. J Fluid Mech 586:1–39
49. Zhong Q, Hussain F, Fernando HJ (2018) Quantification of turbulent mixing in colliding gravity currents. J Fluid Mech 851:125–147
50. Ermanyuk E, Gavrilov N (2005) Interaction of an internal gravity current with a submerged circular cylinder. J Appl Mech Tech Phys 46:216–223
51. Gonzalez-Juez E, Meiburg E, Constantinescu G (2009) Gravity currents impinging on bottom-mounted square cylinders: flow fields and associated forces. J Fluid Mech 631:65–102
52. Cenedese C, Adduce C (2008) Mixing in a density-driven current flowing down a slope in a rotating fluid. J Fluid Mech 604:369–388
53. Theiler Q, Franca MJ (2016) Contained density currents with high volume of release. Sedimentology 63(6):1820–1842
54. Ottolenghi L, Adduce C, Inghilesi R, Roman F, Armenio V (2016) Mixing in lock-release gravity currents propagating up a slope. Phys Fluids 28(5)

Authors and Affiliations

Giovanni Di Lollo[1] · Maria Rita Maggi[1] · Claudia Adduce[1]

✉ Claudia Adduce
claudia.adduce@uniroma3.it

Giovanni Di Lollo
giovanni.dilollo@uniroma3.it

Maria Rita Maggi
mariarita.maggi@uniroma3.it

[1] Department of Civil, Computer Science and Aeronautical Technologies Engineering, Roma Tre University, Via Vito Volterra, 62, 00146 Rome, Italy